ACES Asian Chemical Editorial Society

doi.org/10.1002/asia.202400622

CHEMISTRY AN ASIAN JOURNAL Research Article

www.chemasianj.org

Phosphorous – Containing Activated Carbon Derived From Natural Honeydew Peel Powers Aqueous Supercapacitors

Manickam Minakshi,*[a] Achini Samayamanthry,[a] Jonathan Whale,[a] Rob Aughterson,[b] Pragati A. Shinde,[c] Katsuhiko Ariga,[c, d] and Lok Kumar Shrestha*[c, e]

The introduction of phosphorous (P), and oxygen (O) heteroatoms in the natural honeydew chemical structure is one of the most effective, and practical approaches to synthesizing activated carbon for possible high-performance energy storage applications. The performance metrics of supercapacitors depend on surface functional groups and high-surface-area electrodes that can play a dominant role in areas that require high-power applications. Here, we report a phosphorous and oxygen co-doped honeydew peel-derived activated carbon (HDP-AC) electrode with low surface area for supercapacitor via H_3PO_4 activation. This activator forms phosphorylation with cellulose fibers in the HDP. The formation of heteroatoms stabilizes the cellulose structure by preventing the formation of levoglucosan ($C_6H_{10}O_5$), a cellulose combustion product, which would otherwise offer a pathway for a substantial degradation of cellulose into volatile products. Therefore, heteroatom doping has proved effective, in improving the electrochemical properties of AC-based electrodes for supercapacitors. The specific capacitance of HDP-AC exhibits greatly improved performance with increasing carbon-to-H_3PO_4 ratio, especially in energy density and power density. The improved performance is attributed to the high phosphorous doping with a hierarchical porous structure, which enables the transportation of ions at higher current rates. The high specific capacitance of 486, and 478 F/g at 0.6, and 1.3 A/g in 1 M H_2SO_4 electrolyte with a prominent retention of 98.5% is observed for 2 M H_3PO_4 having an impregnation ratio of 1:4. The higher yield of HDP-AC could only be obtained at an activation temperature of 500 °C with an optimized amount of H_3PO_4 ratio. The findings suggest that the concentration of heteroatoms as surface functional groups in the synthesized HDP-AC depends on the chosen biomass precursor and the processing conditions. This work opens new avenues for utilizing biomass-derived materials in energy storage, emphasizing the importance of sustainable practices in addressing environmental challenges and advancing toward a greener future.

Introduction

Energy plays a pivotal role in human development, with its demand escalating alongside population growth, economic expansion, and technological progress, particularly evident since the onset of the Industrial Revolution.[1] Moreover, human activities are affecting the climate, and global emissions during the past years have risen, leading to global warming due to the greenhouse effect. Globally, climate change is a complex intergovernmental issue with many biological, environmental, sociopolitical, and socioeconomic aspects.[2] These aspects must be addressed to achieve a sustainable energy future with minimal environmental impact.[3–4] Employing renewable energy sources and technology vastly and efficiently can combat climate change and the energy crisis.[5] According to the International Renewable Energy Agency's (IRENA) 1.5 °C scenario, the share of global energy from renewable sources needs to increase from 16% in 2020 to 77% by 2050.[6] However, due to their variable and intermittent nature, integrating renewable sources like wind and solar energy is challenging.[4–5] Energy storage has been identified as a flexible, sustainable, and cost-effective solution for storing excessive renewable energy and using it during times of demand.[7–8] If countries continue to double the proportion of renewable energy in the global energy grid, the total energy storage capacity is expected to triple by 2030.[6]

Energy storage technologies available for large-scale applications can be categorized into thermal, electrochemical,

[a] M. Minakshi, A. Samayamanthry, J. Whale
Engineering and Energy, Murdoch University, WA 6150, Australia
E-mail: minakshi@murdoch.edu.au

[b] R. Aughterson
Australian Nuclear Science and Technology Organization, NSW 2232, Australia

[c] P. A. Shinde, K. Ariga, L. Kumar Shrestha
Research Center for Materials Nanoarchitectonics (MANA), National Institute for Materials Science (NIMS), Tsukuba 305 0044, Japan

[d] K. Ariga
Department of Advanced Materials Science, Graduate School of Frontier Sciences, The University of Tokyo, 5-1-5 Kashiwanoha, Kashiwa, Chiba 277-8561, Japan

[e] L. Kumar Shrestha
Department of Materials Science, Institute of Pure and Applied Sciences, University of Tsukuba; 1-1, Tennodai, 305-8573 Tsukuba, Ibaraki, Japan
E-mail: SHRESTHA.Lokkumar@nims.go.jp

Supporting information for this article is available on the WWW under https://doi.org/10.1002/asia.202400622

kinetic, and mechanical.[8] Among the available storage technologies, in order to meet the increasing demand for flexible, lightweight, and compact electronic devices, extensive research has been conducted on electrochemical energy storage.[7] Supercapacitors show great promise for applications in stationary large-scale electrochemical energy storage systems, portable devices, and electric vehicles due to their unique characteristics of having high specific power, long cycle life with excellent storage retention, and fast charge and discharge. In general, two types of storage mechanisms exist for supercapacitors, one involves an electrochemical double-layer capacitor (EDLC) based on charge absorption and desorption at the carbon electrode/aqueous electrolyte interface and does not exhibit a Faradic reaction over the potential range of operation, whereas, the other is based on the pseudocapacitor principle in which the energy stored is based on surface redox processes / faradaic charge transfer reactions between transition metal oxides or hydroxides and aqueous electrolyte.[9–10] Regardless of the mechanism, however, electrode materials play a pivotal role in determining electrochemical performance. The electrochemical storage depends on the electrode's effective surface area, pore size, conductivity, and surface functional groups.[11] Due to this, significant efforts are being made to develop high-performance electrode materials to meet the increasing demands of emerging technologies. Among the high-performance electrodes, carbon-based materials have gained great attention due to their low cost, superior conductivity, high chemical and thermal stabilities, and cycling stability.[12–14] The widespread use of carbon materials, however, stems from expensive fossil fuel-based precursors (coal, lignite, petroleum coke, and asphalt) and requires an energy-intensive synthesis process that eventually results in marginal performance metrics.

To address these issues, different types of biomass have recently been widely researched and reported as viable feedstocks in the synthesis of carbon materials due to their sustainable, green resource, cost, tunable porosity, and renewable nature.[15–20] The biomass-derived carbon can inherit the structure by tuning the functional surfaces during the carbonization process resulting in the product (activated carbon) delivering high capacitance and long-term stability at low cost. The obtained electrochemical performance is often correlated with the physicochemical properties of the chosen carbon precursors. The synthesis of biomass-derived carbon involves carbonization followed by activation. Among the various activation types, chemical activation is preferred as this facilitates the effective conversion of the precursor to activated carbon. Chemical activating agents such as NaOH, KOH, $ZnCl_2$, and H_3PO_4 are commonly used,[15,16,20–23] in which the activating agents will be introduced into the interior of the biomass precursor particles during the impregnation step that hinders the contraction of the particles while also reducing the release of volatile compounds.[24–25] The pore size distribution of the activated carbon is reported to depend on the ratio of a biomass precursor chemical to activator (*termed* "impregnation ratio").[25] Nevertheless, all these agents give rise to a porous structure with some differences seen between them. The overall number of micropores and mesopores is altered by acidic activation using phosphoric acid (H_3PO_4), a more cost-effective approach that can produce a significant percentage of yields at the optimum amount.[26–27] The H_3PO_4 agent helps to obtain the cross-linked structure of carbonaceous material and promotes the pyrolytic transformation of the starting material. Table 1 outlines the materials[28–32] used as precursors for synthesizing activated carbon where H_3PO_4 acid has been used as an activating agent in the chemical activation process. The table illustrates the processing conditions and impact of phosphoric acid on the activation process of biomass carbon materials. Based on this outlook, we have demonstrated the ability to tune the structure having heteroatoms doping.

Activated carbon derived from a range of biomass precursors[15–16,18,20–22,33] as supercapacitor electrodes with their characteristics are tabulated in Table 2. Besides, various other types of biomass materials have also been used as the precursors, ranging from botanic-derived, algae-derived to animal-derived biomass such as soybean, catkin stems, microalgae, seaweeds, egg white (chicken), crab and shrimp shells, human hair, honey, etc.[12,24] A significant gap in the current research landscape lies in the lack of exploration into honeydew as a potential precursor for activated carbon in supercapacitor applications. Honeydew is a popular fruit worldwide (*Cucumis melo Inodorous group*), which is a member of the Cucurbitaceae family,[34] and its non-edible part (rind) is discarded in more significant amounts (around 10 million tonnes of waste per year worldwide) without proper use. HDP precursors have a low lignin content (8.2 %), cellulose (25.42 %), and hemicellulose (36.85 %). As a result, only low acid concentration and mild carbonization temperature are required to synthesize AC. Despite the promising results exhibited by watermelon-derived activated carbon[35] (having a surface area of 2277 m^2/g and gravimetric specific capacitance of 333.42 F/g), to the best of our knowledge, no study has been reported on HDP except scant work done on rockmelon fruit peel as natural waste. A few works have been conducted on the synthesis of HDP-derived AC as an absorbent and its performance in the elimination of harmful chemicals but no reports for supercapacitor applications.[14,36] Interestingly, the honeydew fruit contains several elements including phosphorous, which may enhance the carbon material's electron-transfer properties, making it a potential electrode for supercapacitors. Therefore, these results inspired the authors to map HDP as a waste-to-wealth-based approach to have a cost-effective electrode.

Experimental

Materials

The honeydew melon-type fruit was purchased from the local market in Subiaco, Western Australia. The following materials: H_3PO_4 acid, polyvinylidene fluoride (PVDF), carbon black, N-methyl-2-pyrrolidone (NMP), and graphite carbon collector (0.25 mm thickness) were obtained from the ChemSupply. The reagent used was analytical grade, and used as received. The peeled outer skin (rind) of the honeydew fruit was used as a precursor to prepare the activated carbon.

Table 1. Various chemically activated biomass-derived AC using acid activator H_3PO_4 reported in the literature.

Biomass precursors [Ref.]	Carbonization	Activation	Electrolyte	Specific Surface Area (SSA) m^2/g	Specific capacitance F/g
Olive stone[28]	Carbonized with acid impregnation 1:4 ratio for following concentrations, H_3PO_4 3 °C/min 500 °C for 2 h, N_2 200 mL/min		–		Not reported for supercapacitors
	H_3PO_4 wt% = 60				
	H_3PO_4 wt% = 70				
	H_3PO_4 wt% = 80				
Cow dung[29]	400 °C for 4 h (Muffle furnace using a clay-sealed graphite crucible to create vacuum environmental conditions)	Activated with H_3PO_4 acid impregnation 1:4, for following temperatures 2 hrs in a muffle furnace	6 M KOH		
		600 °C		489	148 @ 5 mV/s
		700 °C		984	215 @ 5 mV/s
		800 °C		1860	294 @ 5 mV/s
		900 °C		2457	347 @ 5 mV/s
Polyaniline[23]	Carbonization after acid impregnation	4 h in N2 with H_3PO_4 for following temperatures at a heating rate of 5 °C min	6 M KOH		
		700 °C		173.4	137.2
		800 °C		353.0	154.4
		900 °C		260.8	129.1
Olive residues[30]	300 °C for 2 h, N2 (300 cm^3/min)	1:4 ratio with H_3PO_4, 300 °C for 2 h, N_2 and followed by at 700 °C 2 h, N_2	1 M H_2SO_4	771	176 @ 250 mA/g
			1 M Na_2SO_4		130 @ 250 mA/g
Rose Branch[31]	Carbonization after acid impregnation: mixed with 9% H_3PO_4. Carbonize at 210°C for 2 h.	1:3 H_3PO_4 450 °C at a rate 5 C/min for 1 h, N_2 50 ml/min	1 M Na_2SO_4	1803	178 @ 0.2 A/g
	Carbonization with water impregnation. Carbonize at 210 °C for 2 h	1:3 H_3PO_4 for 450 °C 1 h 5 C/min, N2 50 ml/min		1079	154 @ 0.2 A/g
	Carbonization without acid impregnation Carbonize 210 °C for 2 h.	1:3 H_3PO_4 for 450 °C 1 h 5 C/min, N2 50 ml/min		1221	136 @ 0.2 A/g
Hazelnut shell[32]	Carbonization after acid impregnation	1:1 ratio H_3PO_4 heated at 600 °C for 1.5 h 3 °C/min, N2 200 ml/min	6 M KOH	966	338 @ 0.2 A/g

Table 2. Summary of biomass-derived AC materials as SCs in aqueous electrolytes.

Biomass precursors [Ref.]	Carbonization	Activation	Electrolyte	SSA m^2/g	Specific Capacitance F/g
Coffee grounds[22]	–	1:1 ratio $ZnCl_2$ 5 K/min 1173 K for 1 h, in N_2	1 M H_2SO_4	1019	368 @ 0.05 A/g
Apricot shell[21]	500 °C	1:2 ratio NaOH 700 °C for 1 h, in N_2	6 M KOH	2074	336 @ 1 mV/s
Rice husk[16]	–	1:4 ratio $ZnCl_2$ 1123 K 5 K/min, for 1 h, in N_2	6 M KOH	1768	245 @ 0.05 A/g
Poplar wood[33]	900 °C for 6 h, in N_2	1:8 ratio HNO_3, 8 h	2 M KOH	416	234 @ 5 mA/cm^2
Lotus calyx[20]	750 °C 10 °C/min for 3 h, in N_2	1:2 ratio KOH simultaneous	6 M KOH	798	223 @ 1 A/g
Mango seed[15]	600 °C, 5 °C/min for 3 h, in N_2	1:3 ratio KOH 1100 °C 5 °C/min for 1 h, in N_2	2 M NaOH	1943.75	135 @ 5 mA/cm^2
Coffee waste[18]	–	Physical activation in N_2 0.5 ml/min	1 M Na_2SO_4	585–981	72 @ 1 A/g

Methodology

A two-stage process was followed to prepare the activated carbon from the HDP precursor. The carbonization stage was the first, and then followed by the chemical activation stage. The HDP was cut into small pieces (as shown in Scheme 1), and washed with deionized water to remove dust and other impurities. Then, the HDP was dried in the shade and transferred to the oven to dry at 80 °C overnight to reduce moisture content. The dried HDP was ground into small particles using a kitchen blender and screened through a mesh sieve 250 μm (Sample A1). Then, the powdered sample was put into the muffle furnace to reach 300 °C with a heating rate of 2.5 °C/min for 4 h. This was labeled as a Honeydew peel-derived carbonized sample (Sample A2).

In the subsequent stage, chemical activation is performed. This is carried out by thermal treatment of the carbonized material mixed with the dehydrating agent. As the chemical activating agent (H_3PO_4 in our work) and activation temperature determine the yield of the final product (i.e.) activated carbon, we varied the impregnation ratio and the activation temperature during the synthesis. Carbonized sample and H_3PO_4 (85 %, chem Supply) ratios at different concentrations were intimately mixed in a solution. The prepared HDP-AC samples under various conditions are tabulated in Table 3. The slurry was oven-dried and finally put into the muffle furnace at 500 °C at a heating rate of 2.5 °C/min for 1 h. After the activation, the samples were cooled to room temperature. The sample was washed to remove the excess acid with deionized water until the pH value became neutral. Then, the HDP-AC sample was oven-dried at 60 °C for 12 h.

Physical Characterization of HDP-AC

The structural determination of the synthesized HDP-AC samples for different carbonised HDP to H_3PO_4 ratios (shown in Table 3) at synthesis temperatures of 500 °C was carried out by X-ray diffraction (Rigaku, Japan) using Cu Kα radiation. The Fourier-transform infrared (FT-IR) method with a NICOLET iS20 instrument (Thermo-Fisher Scientific, Waltham, MA, USA), and Raman Spectroscopy with an NRS-3100 (JASCO, Tokyo, Japan) instrument at the excitation wavelength of neon laser 532.09 nm, were used for identifying the surface functional groups and nature of carbon present in the bulk and surface of the samples. Each sample was analyzed on at least three different surface locations at a depth of 3 μm. A colorimetric method is used for the determination of phosphorous (P) and nitrogen (N) in the selected compositions of HDP-AC samples. The samples are digested in the optimized molarity of H_2SO_4 and the required elements are determined by a photoelectric colorimeter type cell of a dilute aliquot of the sample digest. The morphology and elemental composition on the surface of the synthesized HDP-AC were analyzed using Field Emission Scanning Electron Microscopy (FESEM, Zeiss NEON 40EsB). Transmission electron microscopy (TEM) images were collected using a JEOL 2200FS TEM operated at 200 kV. TEM specimens were prepared by grinding a small amount of HDP-AC powder under ethanol in an agate mortar and pestle and dispensing via pipette onto a holey carbon film supported on a TEM copper mesh grid. Elemental maps were collected in scanning TEM (STEM) mode via X-ray energy dispersive spectroscopy (EDS) using an Oxford X-Max 80 mm^2 detector interfaced with Oxford INCA, version 4.15, microanalysis software. The surface area and pore analysis (SAPA) of the samples were carried out by N_2 adsorption-desorption isotherms at 77 K. The obtained specific surface area was calculated by the Brunauer—Emmett–Teller (BET) method.

Electrochemical Characterization of HDP-AC

For electrochemical measurement, the electrode was prepared by mixing either HDP-AC (75 wt%), carbon black (15 wt%), and polyvinylidene difluoride PVDF (10 wt%) with 0.4 mL of N-Methyl-2-pyrrolidone (NMP) to make a slurry. This was coated on a small piece of graphite sheet (area of coating, 1 cm^2). The loaded active material was around 2 mg in each case. In three-electrode tests, a platinum wire of 10 cm in length and 1 mm diameter in dimension and mercury–mercuric oxide (Hg/HgO) served as the counter and reference electrodes, respectively. In single-electrode tests, HDP-AC served as the working electrode. The cyclic voltammetry and galvanostatic charge-discharge studies of the composites were carried out using SP-150, Bio-Logic Science instruments in 1 M H_2SO_4 electrolyte at room temperature. The chosen H_2SO_4 electrolyte has higher conductivity (35 mSm^2/mol) and ionic radius (2.80 Å for H^+), as opposed to the KOH counterpart, which has the lowest conductivity (5 mSm^2/mol) and ionic radius of 3.31 Å for K^+).

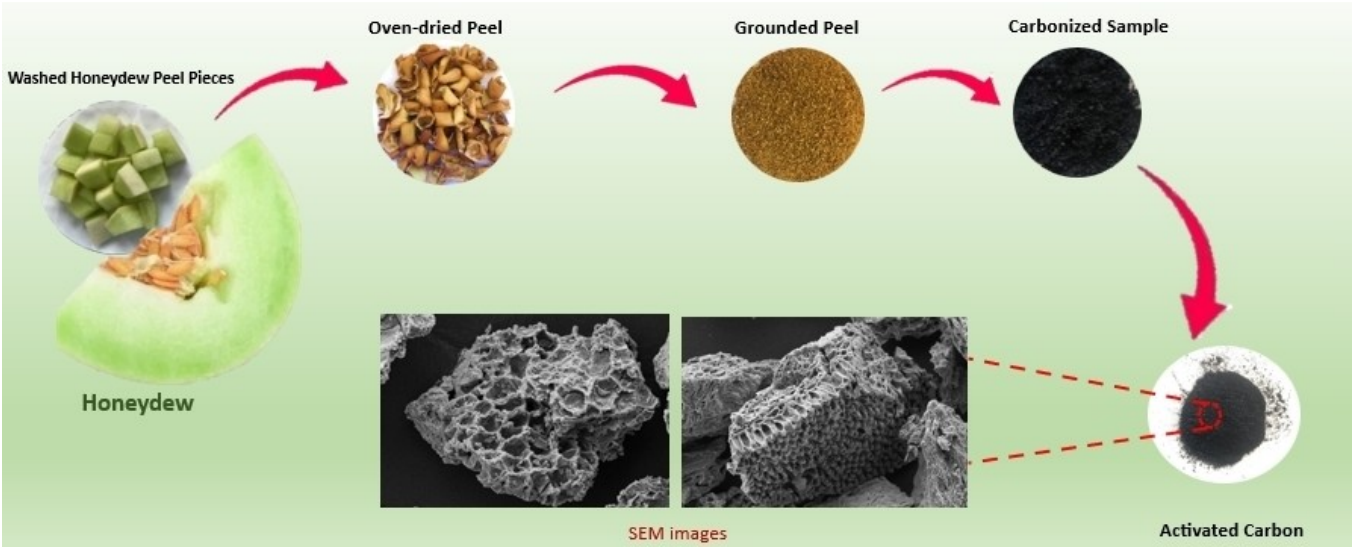

Scheme 1. Schematic synthetic route of activated carbon derived from the honeydew peel (HDP-AC) involving carbonization, and activated process at different synthesis conditions tabulated in Table 3.

Table 3. Chemically treated HDP samples.

Biomass precursors [Ref.]	Voltage (V)	Electrolyte	Current density	Specific capacitance (F/g)	Energy density (Wh/kg)	Power density (W/kg)
Lotus calyx[20]	1	6 M KOH	1 A/g	223	66.8	800
Mango seed[15]	1	2 M NaOH	5 mA/cm^2	135	19	1077
Groundnut Shell[56]	1	6 M KOH	0.5 A/g	220.6	7.64	275
	1.8	0.5 M Na_2SO_4	0.5 A/g	150.4	16.92	451.2
Corn Starch[57]	1	6 M KOH	0.625 A/g	144	19.9	311
Kusha grass (Desmostachya bipinnata)[58]	0.8	6 M KOH	0.7 A/g	218	19.3	277.92
Neem (azadirachta indica)[59]	2	1 M $LiClO_4$	1 mA/cm^2	74.41	10.33	4660
Sunflower Stalk[60]	1	6 M KOH	0.5 A/g	263	35.7	989
Rockmelon Peel[35]	1	1 M KOH	1 A/g	404	29.3	279.78
Bamboo[61]	1	6 M KOH	0.1 A/g	258	>2	>2000
Pine Cone[62]	2	1 M Na_2SO_4	0.1 A/g	137	19	100
Borassus flabellifer flower[63]	0.6	1 M KOH	1 A/g	238.2	–	–
Camellia oleifera shell[64]	1	1 M H_2SO_4	0.2 A/g	374	–	–
	1	6 M KOH	0.2 A/g	266	–	–
Lentinus edodes[65]	1	1M H_2SO_4	0.2A/g	389	54.03	–
Peanut shell[66]	1	1 M H_2SO_4	0.5 A/g	340	10.8	106.9
Tamarindus indica Fruit Shell[67]	0.78	1 M KOH	1 A/g	285	–	–
Oil palm empty fruit bunches[68]	1	1 M H_2SO_4	–	150	4.3	173.3
Rice Straw	1	6 M KOH	0.5 A/g	178	–	–
Rice Straw – N doped[69]				324 @N-doped	–	–
Cotton[70]	1	6 M KOH	0.5 A/g	270	18	250
Ginkgo leaves[71]	1	1M H_2SO_4	0.5 A/g	374	45.9	221
Pomelo Peel[72]	1.7	1 M $NaNO_3$	0.5 A/g	43.5	17.1	420
Sugar cane bagasse[73]	1	1 M H_2SO_4	0.25 A/g	~300	5.9	10000
Honeydew Peel HDP (This work)	1	1M H_2SO_4	0.6 A/g	480	66.5	662

Therefore, H_2SO_4 is one of the widely examined aqueous electrolytes. For HDP-AC, the working electrode was cycled between 0 and −1.0 V in 1 M H_2SO_4 electrolyte. The frequency range for electrochemical impedance spectroscopy (EIS) was 10 MHz to 40 MHz with a 5 mV bias voltage.

The specific capacitance was computed from the following equations (from cyclic voltammetry; 1a), and (from charge-discharge; 1b).

$$CS = \int ivdv/2\,\mu m\,\Delta V \tag{1a}$$

where C_s is the specific capacitance in (F/g), i and v are the current and potential in the cyclic voltammetry (CV) test expressed in (A), and (V), respectively, $\int ivdv$ is the integrated area under the CV curve, μ is the scan rate (mV/s), m is the mass of the active material (g), and ΔV is the potential window of CV curve.

$$C_s = \frac{i \times \Delta t}{\Delta V \times m}\ (\mathrm{F/g}) \tag{1b}$$

where i is current in (mA), $\triangle t$ is the discharging time (s), m is the mass of the active material loaded (mg) and ΔV is the potential window of charge/discharge (V). The energy and power density of the device were calculated using the formulas in equations (2–3).

$$E = \frac{1}{2} C_s \frac{\Delta v^2}{3.6}\ (Wh/\mathrm{kg}) \tag{2}$$

$$P = \frac{E \times 3600}{t}\ (\mathrm{W/kg}) \tag{3}$$

where E and P denote the energy density (Wh/Kg), and power density (W/Kg) of the device. The coulombic efficiency of the electrode is calculated by the ratio of the charge delivered from the electrode during discharge to the charge stored on the electrode during charge in the same cycle and the current densities.

Results and Discussion

Physico-Chemical Characterization of HDP-AC

The X-ray diffraction pattern of the HDP-AC selective samples is presented in Figure 1. The raw (pre-carbonized; A1) HDP in

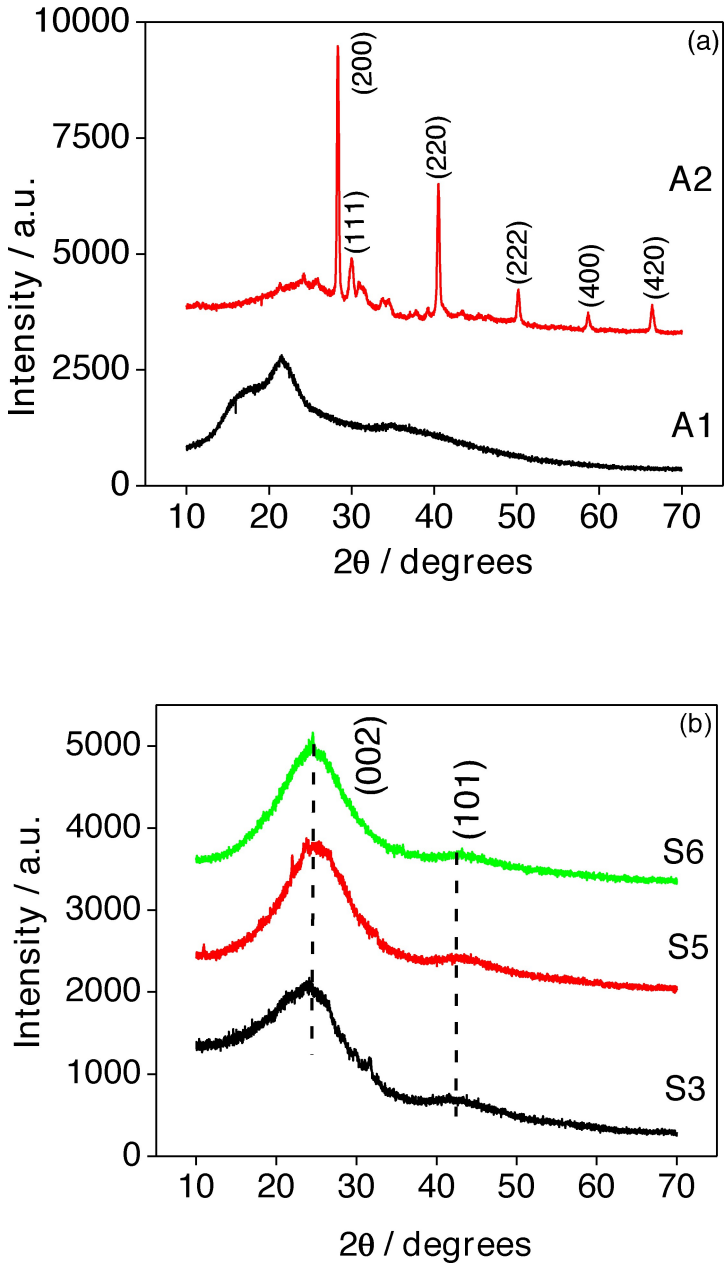

Figure 1. X-ray diffraction patterns for the samples derived from the honeydew peel (HDP-AC) (a) pre-carbonized (A1), carbonized (A2), and (b) activated at different synthesis conditions.

Figure 1a shows two broad peaks at 2θ values 21.4° and 34.5°, which corresponds to the characteristic disordered carbon.[23] For the carbonized HDP sample (A2), surprisingly, there is an evolution of five prominent peaks at 2θ values 28°, 40°, 50°, 58°, and 66° corresponding to the formation of crystalline potassium chloride (KCl). During carbonization, HDP undergoes depolymerization of lignin and other components, followed by dehydration and condensation, leading to the removal of volatiles, and aromatization, with some cross-linking.[37] Honeydew melon is rich in potassium, chloride, and high levels of phosphorous resulting in fruits with thinner and smoother rinds.[38] For carbonized HDP at 300 °C, the decomposition of cellulosic and hemicellulosic components releases the volatile gas with the yield of carbon composites having KCl. In the subsequent stage, for the chemical activation process, the acid activator (H_3PO_4) is intimately mixed with carbonized HDP and heat treated at 500 °C. Above this temperature, the breakdown of phosphate groups resulting in a lower phosphorous content may lead to HDP-AC with reduced porosity. The activation process begins with cellulose depolymerization followed by biopolymer dehydration to produce aromatic rings, leading to the activation of carbon resulting in HDP-AC. During activation, the water-soluble KCl salt might react with HDP under heat treatment, and Cl is released as a gaseous phase while K is melted in solid carbon material producing a porous graphitic carbon.[39] The XRD patterns for all the chemically activated samples, invariable

to the concentration of H_3PO_4 and their impregnation ratios (samples S3, S5, and S6), shown in Figure 1b, and reveal typical disorder structure by having broad peaks at 2θ values shifted to a higher angle at 24.3° and 42.5°. These peaks correspond to the Miller indices (002) and (101) representing graphitic carbon with an amorphous structure.[40] After chemical activation, the 2θ values and peak broadening were not altered. Figure S1 shows the XRD patterns for the lower concentration of activators (samples S1, S2, and S4) which is quite consistent with the diffraction pattern shown in Figure 1, except for shoulder peaks in samples S1 and S2, which could be the traces of KCl residue.

To identify the chemical bonding, and surface functional groups of the synthesized HDP-AC, the selected activated samples were characterized by FT-IR technique. The obtained FT-IR spectra (shown in Figure 2a) of the samples synthesized at higher concentrations (S5 and S6) are more prominent and have similar features with higher intensities than the samples at lower concentrations (S3 and S4). This suggests more oxygen-containing functional groups were formed in the higher concentration of samples S5 and S6, which could absorb less moisture in the available pores of the activated carbon. The consequence of these effects could enhance surface wettability by promoting ion transfer and providing additional storage performance. The absence of any visible bands around the

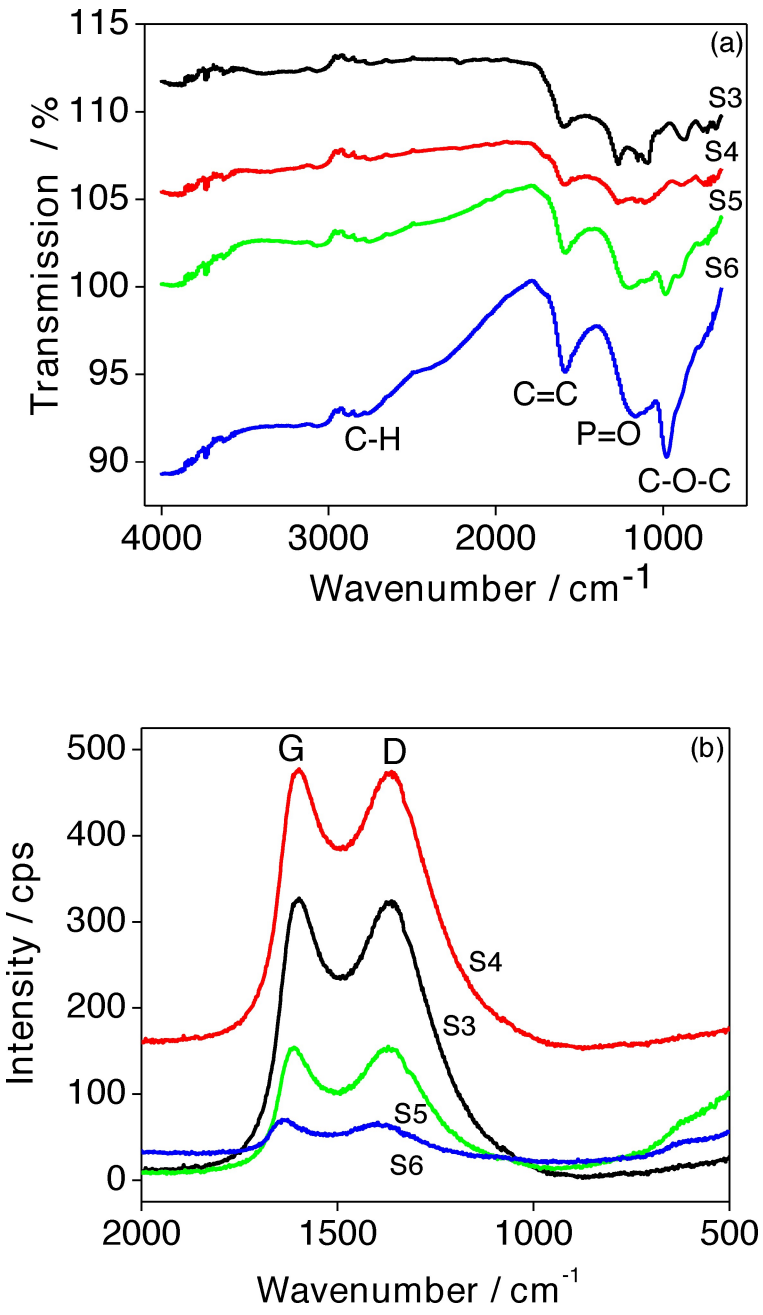

Figure 2. (a) FT-IR, and (b) Raman spectra for the activated carbon samples derived from the honeydew peel (HDP-AC) at different synthesis conditions.

near-IR region (in Figure 2a) indicates there are no O–H functional groups of lignin, and other adsorbed water molecules present on HDP-ACs. Likewise, bands around 2700 cm^{-1} corresponding to C–H stretching vibrations are also less pronounced. The carbonyl group on the HDP-AC exhibits an intense peak observed at 1550 cm^{-1} due to C=C stretching while at 1210 cm^{-1} is due to P=O groups, suggesting the presence of P-heteroatoms coming from the H_3PO_4.[40–41] This could lead to surface functionalized carbon. Further, the strong peak at 1000 cm^{-1} is related to C–O–C stretching that may be present in ethers in HDP. The H_3PO_4 reacts with HDP to create phosphate bonds leading to the formation of functional groups like C–O–PO_3.[42] This group promotes the porous surface and enhances surface functional groups. Therefore, it can be concluded that ion exchange takes place during the synthesis and secure P doping at a stronger concentration of 2 M H_3PO_4, and impregnation ratio 1 : 4 (S6 in Table 3). To determine the presence of phosphorous and quantify, a spectrophotometric colorimetric analysis has been performed on the selected HDP-AC samples. The spectrophotometric method is chosen over spectrometric due to its sensitivity and reliability to analyze small amounts of samples. To avoid any inaccuracies leading to an understated content of elements present, HDP-AC samples are fully digested in the 1 M H_2SO_4 reagent before analysis. The extent of the amount of phosphorous present in the sample shown in Figure S2 is significantly higher for S5 and S6 samples corresponding to 120 mg/g, and 170 mg/g, respectively. Whereas, the presence of nitrogen appears to be fairly constant for S5 and S6 samples. This illustrates the higher amount of activator (H_3PO_4) in S5 and S6 influences phosphorylation and is found to be effective for stabilizing the material.

The Raman analysis of the samples S3–S6 (in Figure 2b) exhibited two intense peaks located at regions 1375 and 1600 cm^{-1} corresponding to the D (disorder) and G (graphitic) peaks, respectively. The distortion of the graphitic structure leads to the evolution of the D-peak. The ratio of the intensities for the D and G peaks (I_D/I_G) was seen to be approximately unity in the S5 (0.95) and S6 (0.96) implying a stronger degree of graphitization while creating more disordered structures favoring the electron transfer process. As reported by Qian et al.,[43] the higher I_D/I_G ratio indicates a higher amount of heteroatom doping for sample S6. The Raman analysis confirms the chemical activation caused disorder by forming defects from the breakage of the sp^2 configuration, possibly due to the formation of functional groups.[44] This could aid the electrochemical activity of the HDP-AC samples.

The incorporation of heteroatom (O, and P) between the cellulose chains, and other functional groups was further visualized by field-emission scanning electron microscopic (FE-SEM) images associated with the elemental dispersive spectra (EDS) technique. The FE-SEM and STEM images of HDP-ACs are shown in Figures 3–5. The pre-carbonized HDP (A1) sample shows an aggregated particle of 10 μm (Figure 3A), having wrinkled layers with irregular surfaces (Figure 3B). The carbonized HDP (A2) shows an evolution of pores on the rough surface of the HDP particle (Figure 3C), forming a round-shaped crystalline-like particle with a size of 2 μm (Figure 3D). The corresponding EDS image shows the crystalline particles are KCl (Figure 6). This is in agreement with the XRD results showing a crystalline pattern for sample A2. H_3PO_4-activated samples at lower concentrations (S3 and S4) exhibit hierarchical porous patterns like egg cartons (Figures 3E–F) and honeycombs (Figures 3G–H) with numerous cavities and canals. These short pits can limit the transportation of ions from the electrolyte. At higher concentrations (S5 and S6) a more compact porous structure is viewed with a smaller surface area, which can provide a feasible pathway for ion transfer. The abundantly available macroporous open structure (Figures 3I–K) can act as buffer space for fast ion transportation and be suitable for high-rate capability.[42] Figure 5 shows transmission electron microscopy (TEM) micrographs (A–C) that further highlight the porous structure, which consists of predominantly amorphous regions. The STEM mapping showed the region consists of P, O, and C. Samples S5 and S6 had a generally similar structure shown in TEM micrographs (Figures 4 and 5), though a crystalline material is found in S6. For sample S6, a corn-shaped porous structure is viewed in Figure 3L. On the surface, rose flower-shaped particles are cascaded into a long chain on the base porous HDP material (Figures 3M–N). Through EDS analysis shown in Figure 7, these cascaded crystal particles are found to be phosphorous. This microstructure with P-heteroatoms was promoted to build high-performance HDP-AC electrodes for supercapacitors. The O/P atomic ratio in the EDS spectra suggests that P and O are co-doped in the carbonaceous matrix. The observed results are similar to those reported for multi-heteroatom-doped ultrathin carbon nanosheets.[45] While comparing S5 and S6, we observe not only the heteroatoms are present but also the constructive pore walls developed in the S6 sample. This developed pore wall resulted in a high yield of sample, whereas, concentrations of H_3PO_4 above the optimum concentration (> S6) resulted in a significantly lower yield because a large part of the cellulosic structure has been degraded.[46–47] The proposed reactions for H_3PO_4 activation during the optimum temperature of 500 °C are given in Eqs (4–6).

$$nH_3PO_4 \rightarrow H_{n+2}P_nO_{3n+1} + (n-1)H_2O \quad (4)$$

$$H_{n+2}P_nO_{3n+1} \rightarrow P_4O_{10} + H_2O \quad (5)$$

$$P_4O_{10} + 2\,C \rightarrow P_4O_6 + 2\,CO_2 \quad (6)$$

Dehydration of H_3PO_4 releases H_2O, and the resulting phosphorous pentoxide (P_4O_{10}), a strong active oxidant, interacts with carbon to create new pores and widen existing ones, releasing CO_2 gas.[24,48] This phosphorylation of cellulose is the heteroatom visualized in the SEM images (Figure 3L–N) and the EDS spectra support this argument. Due to these reasons, the activated samples showed a low surface area of 3 m^2/g. The nitrogen sorption isotherms of HDP-AC samples (S4–S6) are shown in Figure 8. The isotherms for S4 exhibit type II with a hysteresis loop at a relative pressure between 0.4 and 0.7. The isotherm for S4 is characterized by a less sharp increase in volume at low relative pressure indicating the presence of

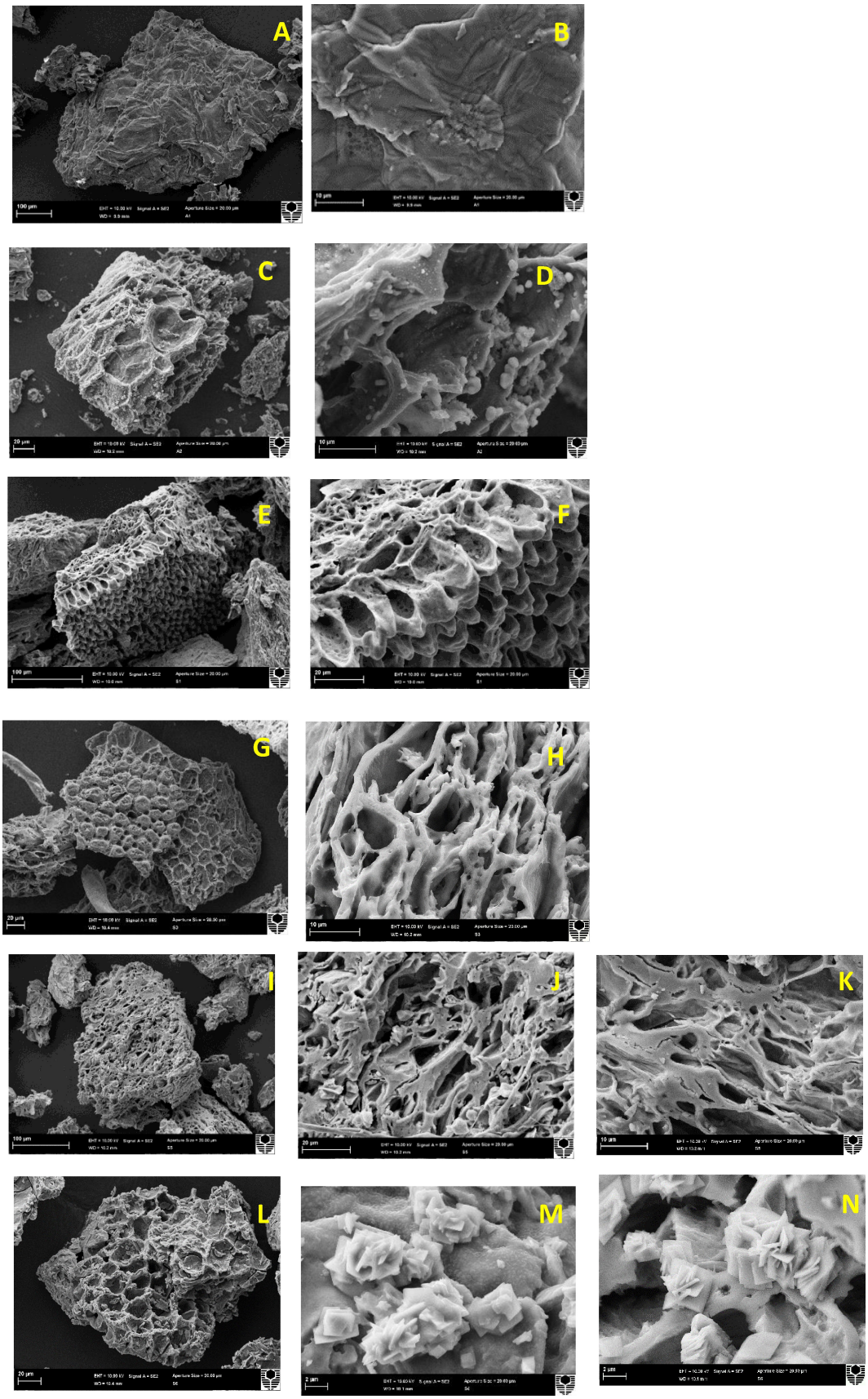

Figure 3. FE-SEM images of (A–B) A1, (C–D) A2, (E–F) S3, (G–H) S4, (I–K) S5, and (L–N) S6 HDP-AC samples synthesized at various conditions.

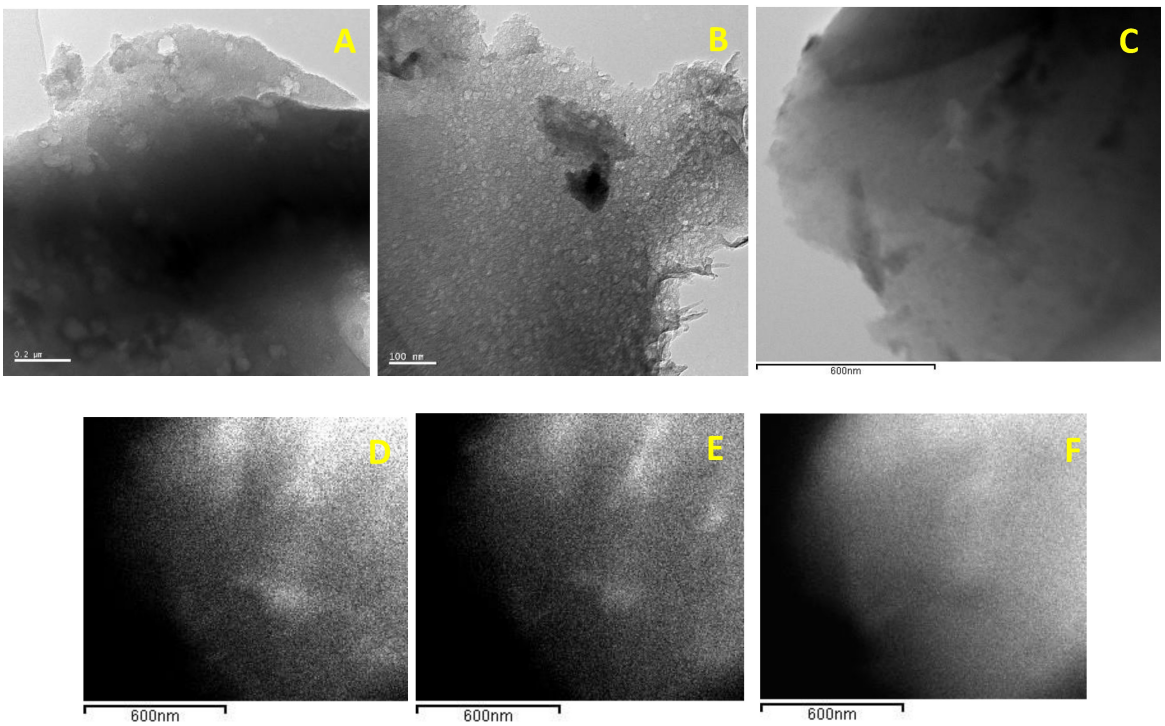

Figure 4. Transmission electron micrographs (TEM) of the HDP-AC S5 sample showing amorphous porous regions. Images (A–C) are scanning TEM (STEM) images, with (D–F) showing corresponding X-ray energy dispersive spectroscopy (EDS) maps (phosphorus, oxygen, and carbon) from regions of interest in (C).

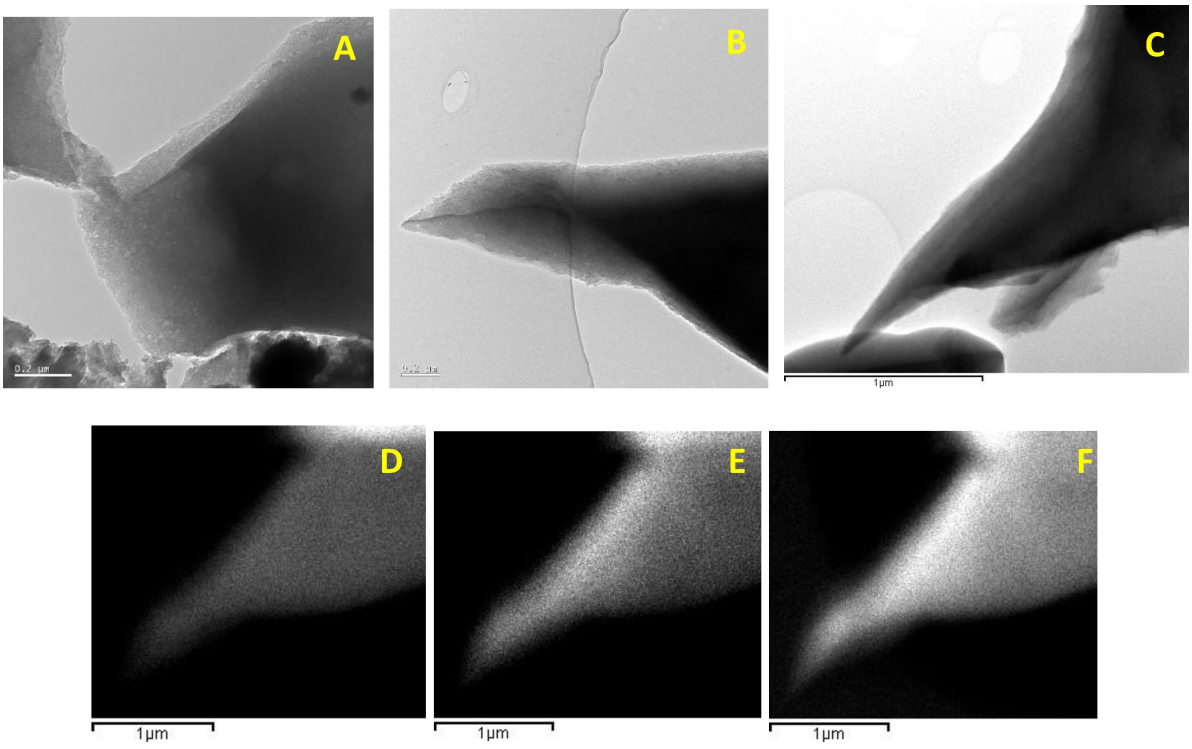

Figure 5. Transmission electron micrographs (TEM) of the HDP-AC S6 sample showing amorphous structure having crystalline regions. Images (A–C) are scanning TEM (STEM) images, with (d–f) showing corresponding X-ray energy dispersive spectroscopy (EDS) maps (phosphorus, oxygen, and carbon) from regions of interest in (C).

macropores.[49] The slow but continuous increase over a wide range of P/Po with a less defined hysteresis was observed for S5 while a flat curve without any hysteresis loop was observed for the S6 sample corresponding to isotherm type Ib and Ia,

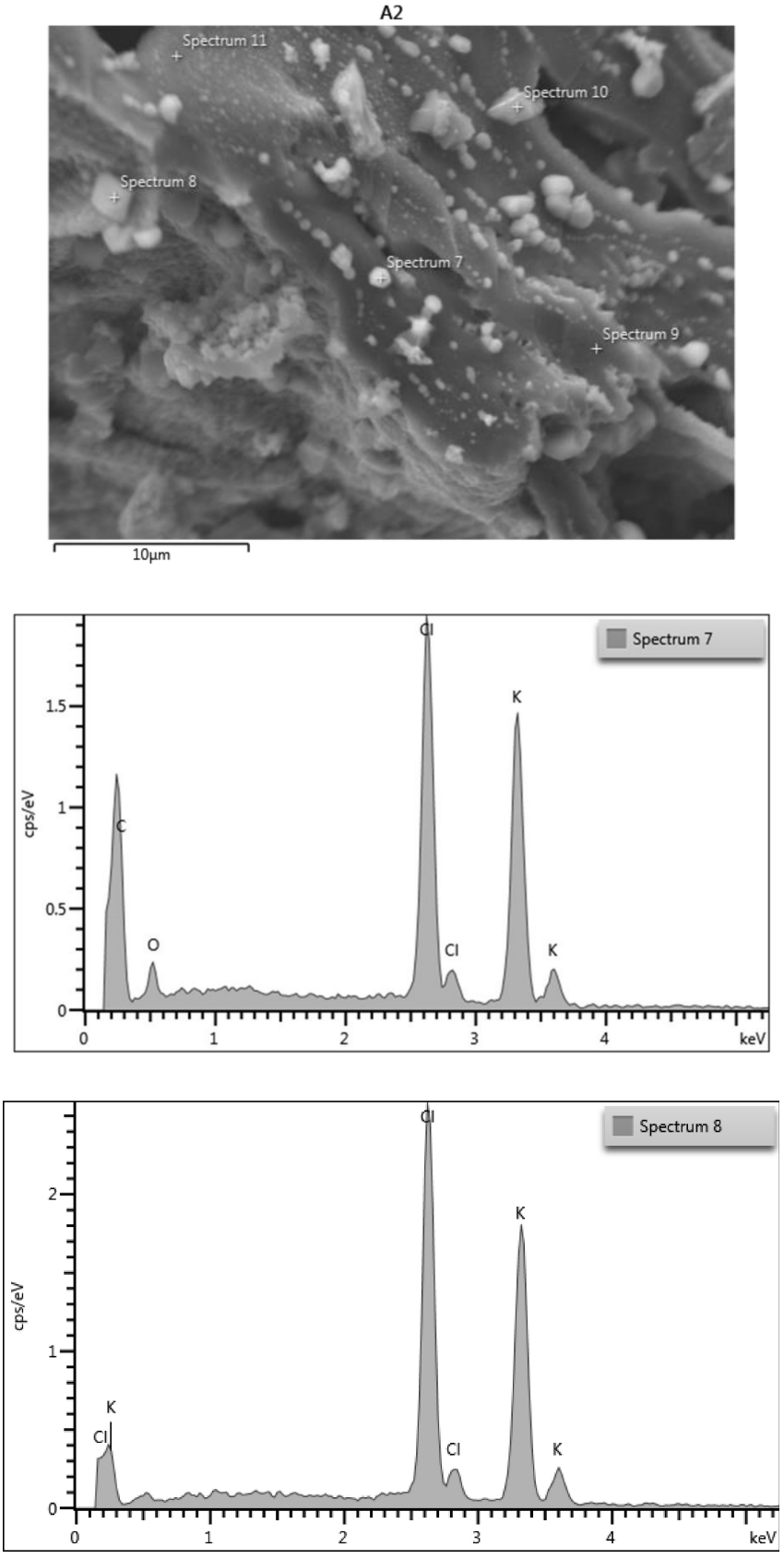

Figure 6. FE-SEM image of the HDP-AC sample A2 showing regions with KCl and the corresponding EDS images confirm the presence of K and Cl.

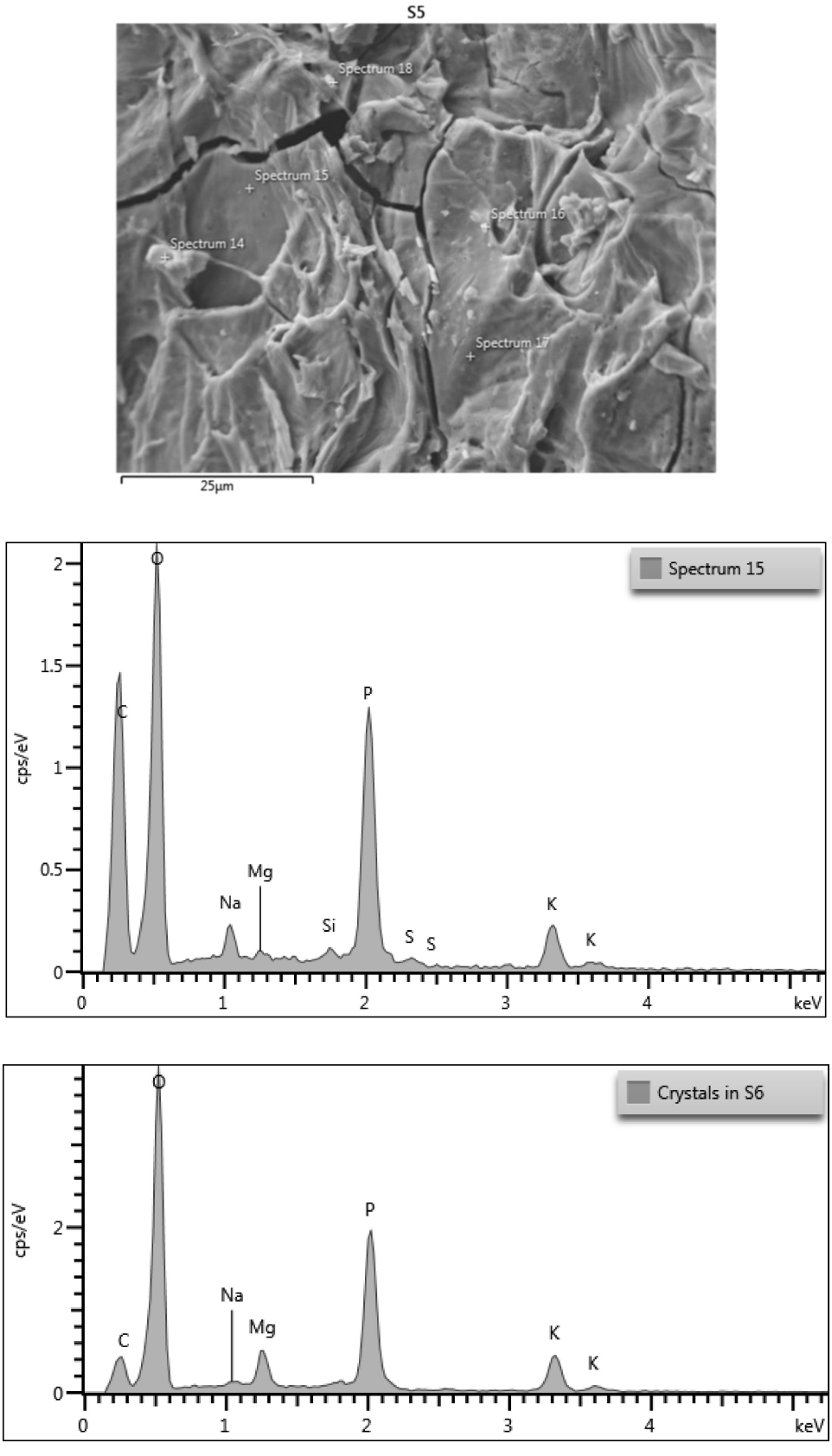

Figure 7. FE-SEM image of the HDP-AC sample S5 with the region focussed (spectrum 15), and the crystals seen for sample S6 in Fig. 3 (M–N) showing regions with phosphate cluster and the corresponding EDS images confirm the presence of K.

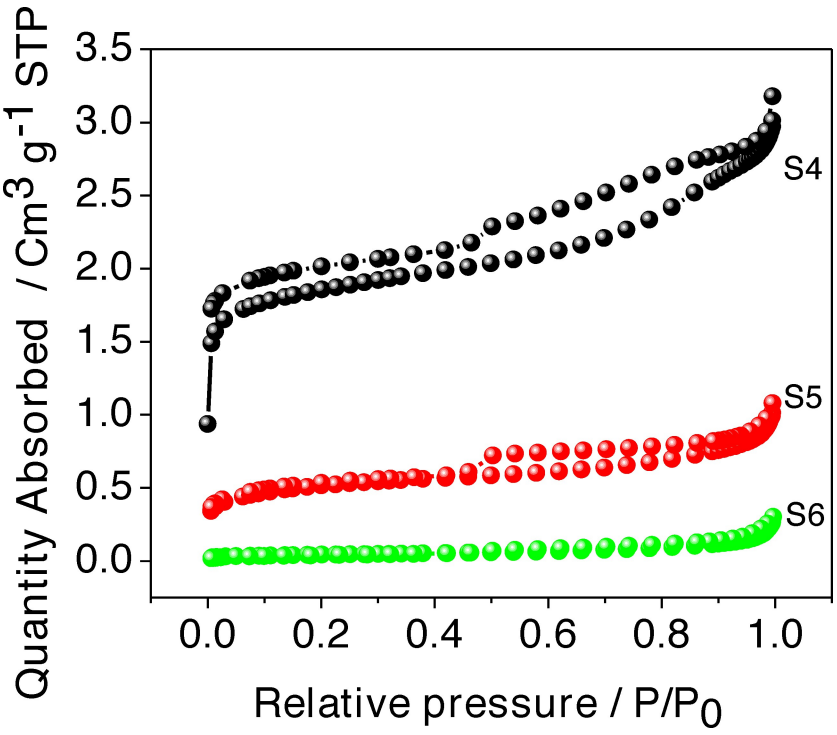

Figure 8. Nitrogen adsorption-desorption curves for the activated carbon samples derived from the honeydew peel (HDP-AC) at different synthesis conditions

respectively. The barely defined knee and long plateau which extends to P/Po = 1.0 indicate microporous powders with no or fewer mesopores.[49] The increasing concentration and ratio of H_3PO_4 impregnation shifts the isotherms downward to lower surface area values with a less-defined hysteresis loop. The quantity of adsorption is also relatively very low, due to the HDP-AC sample's low surface area. The BET (Brunauer–Emmet–Teller) surface area (S_{BET}) of the selected HDP-AC samples listed in Table S1 is not high compared with the values reported in Tables 1 and 2 for various biomass precursors. However, it should be noted that most of the surface area values reported in Tables 1 and 2 are synthesized at different conditions and higher temperatures. Due to this, the tabulated specific surface area (SSA) values and our values cannot be compared. In our work, we cannot find a correlation between the S_{BET} of HDP-AC powders and the obtained specific capacitance values.

Table S1 shows that both the S_{BET} and average pore volume for sample S1 are relatively higher than those of HDP-AC samples at other higher concentrations of activator (S3, S5, and S6). Specifically, S1 has a BET surface area of 224.4539 m^2/g and a pore volume of 0.076194 cm^3/g while S6 has a much lower BET surface area of 3.0049 m^2/g and a pore volume of 0.000867 cm^3/g. However, the specific capacitance value for S6 is the best-performed sample as detailed in the following section (electrochemical characterization). Our experimental results suggest that increased concentrations of activator (sample S6) result in materials with micropores (< 2 nm) containing heteroatom residues, leading to defects and the formation of turbostratic carbons. The introduction of heteroatoms results in functional groups on the carbon surface of S6, which could have altered the surface properties and reduced nitrogen adsorption. Hence, the formation of turbostratic carbon led to a disordered structure, in which the surface area is not high.

Electrochemical Characterization of HDP-AC

Acid vs. Alkaline Electrolytes

To mitigate safety concerns, aqueous electrolytes are the natural choice in the energy storage field. Water is much cheaper than organic solvents, exhibits high conductivity, is easier to purify, and has fewer recycling/disposal issues.[9] Aqueous supercapacitors featuring low-cost, non-flammable, safe, and sustainable water-based electrolytes provide reliability and cost advantages over competing organic chemistries, as they do not require complex storage management systems. The electrochemical performance of HDP-AC is verified in acid (1 M H_2SO_4) and alkaline (1 M KOH) electrolytes.

The preliminary cyclic voltammetry (CV) curves are shown in Figure 9. Both CV curves are characterized by an electrochemical double layer (EDLC) behavior in a 1 V window, but the acid in the positive potential is slightly distorted with the pseudocapacitive response while the alkaline in the negative region is ideal capacitive behavior. The higher conductivity and large ionic mobility of H^+ in acid H_2SO_4 aid in fast charge transfer during the electrochemical redox reactions, and the smaller hydration sphere radius of H^+ between water molecules by hydrogen bond supports more ion adsorption at the

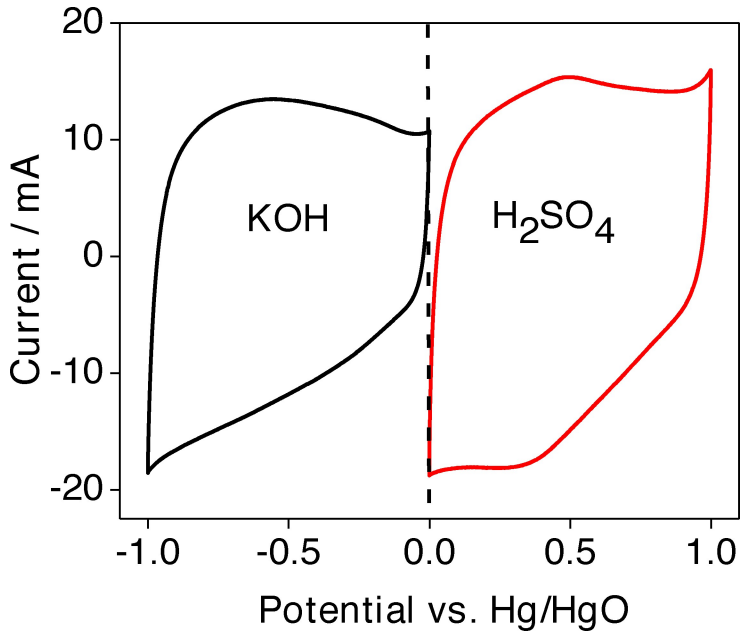

Figure 9. Cyclic voltammetric (CV) curves for the activated carbon sample (S6) derived from the honeydew peel (HDP-AC) tested at 1 M KOH and 1 M H_2SO_4 aqueous electrolytes.

electrolyte/electrode interface to enhance the Faraday reaction.[50] Therefore, due to the smallest hydrated ions and highest acidic conductivity and ionic mobility, the supercapacitor with H_2SO_4 as the electrolyte shows the largest specific capacitance over the counterpart of the alkaline KOH electrolyte. Comparing the electrolyte anions (OH^- and SO_4^{2-}), hydroxide ions show higher conductivity (~200 $cm^2 \Omega mol^{-1}$) and ionic mobility (2×10^{-6} $cm^2 S^{-1} v^{-1}$) than sulfate ions.[9] The anionic size of SO_4^{2-} ions (1.49 Å) is larger compared to OH^- ions (1.10 Å). However, the destruction caused by the large-size cation such as K^+ insertion and extraction (or adsorption and desorption) into/from the HDP-AC electrodes during the redox reactions is greater than the H^+. Nevertheless, the faradaic interactions between the ions in the chosen electrolytes and surface functional groups of the HDP-AC give rise to almost similar behavior. Compared with the capacitances of the HDP-AC electrodes using these two electrolytes with the same concentration, the maximum current response and specific capacitance are obtained when using the H_2SO_4 electrolytes. Based on this preliminary electrochemical work, the acid H_2SO_4 electrolyte is chosen for all the chemically activated samples HDP-AC (S1–S6).

HDP-AC in 1 M H_2SO_4 Aqueous Electrolyte

The CV technique was used to assess all the samples (S1–S6) and the profiles are shown in Figure 10 for different sweep rates ranging from 5–100 mV/s. The CV curves of the HDP-AC sample (S1) impregnated with a low ratio and lower concentrations of H_3PO_4 did not exhibit a high current response, this might be due to the insufficient pores developed for the activation process to occur. The shape of the CV curve is partly elliptical due to the characteristic nature of the synthesized carbon. However, samples (S2–S3) showed an increase in the current response while retaining the shape of the EDLC curve at high potential scan rates, revealing their good rate performances in acid electrolytes. All curves exhibit the typical rectangular shape indicating the capacitive performance.[51] For higher concentrations with high ratios (S4–S6), the current response was significantly increased with a well-defined rectangular shape with a small hump during the oxidation. Among all the six samples analyzed and shown in Figure 10, obviously, the CV curve of the S6 electrode displays the largest area under the curve, which implies the highest current response led to the highest capacitance. The CV shapes even at higher sweep rates up to 100 mV/s still retain the shape indicating excellent electrochemical capacitive properties. The higher content of C–O–P heteroatom in the S6 HDP-AC electrode could enhance the defects and active sites,[40] which contributes to the observed higher specific capacitance. The CV curves of the samples (S5–S6) with higher concentration also showed pseudocapacitive behaviour with a slightly distorted rectangular curve. This could be due to the presence of both oxygen functionalities and C–P groups influencing the surface-controlling process, resulting in pseudo-capacitive behavior.[52] The introduction of heteroatoms into the HDP-AC can form a protective oxide layer on the surface that inhibits the formation of any unstable surface groups enabling cycling performance. In the potential window of 1.0 V, the best-performed sample S6 with a higher concentration ratio showed the highest capacitance of 612, 572, 527, 490, 480, 455, and 412 F/g at the respective scan rates 5, 10, 20, 40, 60, 80, and 100 mV/s. The capacitance obtained from the cyclic voltammetric curves is calculated using Eq. 1a. The highest capacitance is achieved for the S6 sample with the lowest surface area. It is quite a

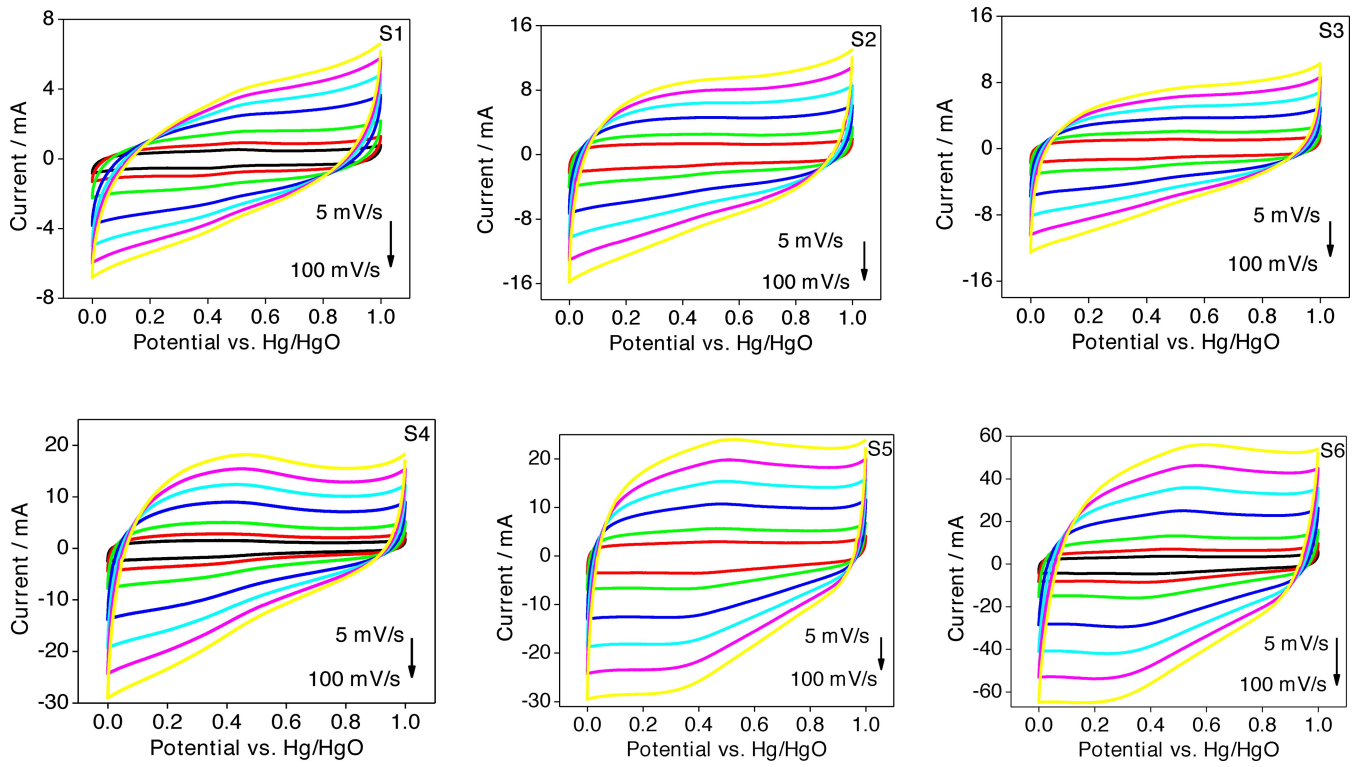

Figure 10. Cyclic voltammetric (CV) curves for the activated carbon sample derived from the honeydew peel (HDP-AC) tested in $1MH_2SO_4$.

common practice not to compare the specific capacitance values obtained from the different techniques such as CV and charge-discharge (CD) curves. However, it is an overall indication that the S6 sample shows improved electrochemical behavior.

The galvanostatic charge-discharge curves for samples (S1–S6) are shown in Figure 11. The symmetric charge-discharge is seen for samples (S1–S3) and the quasi-triangular curve is seen for samples (S4–S6) at various current densities indicating a pseudocapacitive (charge transfer) behavior and overall good reversibility is observed in H_2SO_4 electrolyte. The symmetric shape characterized by EDLC behavior does not require very high ion mobility while the quasi-triangular shape requires fast transfer of ions for quick redox processes at the electrode/electrolyte interface. The presence of H^+ with a high mobility enhanced rapid and efficient charge propagation resulting in improved capacitance. The specific discharge capacitance for S1, S2, S3, S4, S5, and S6 are found to be 45, 90, 75, 180, 188, and 486 F/g, respectively at 1.3 A/g. The specific capacitance of sample S6 was 480, 485, 450, and 425 F/g at the current densities of 0.6, 1.3, 6.6, and 13.3 A/g. The best capacitance value is obtained for 1.3 A/g (i.e. 485 F/g), however, to test its suitability for high-power applications without compromising the capacitance, the median value of 3.3 A/g is chosen for long-term cycling. The high capacitance and excellent rate capability were achieved for sample S6. Based on the performance metrics, the samples can be categorized into three tiers (in Figure 12a), S1–S3 fall in the first tier while the S4–S5 and S6 fall into the second and third tier, respectively. Interestingly, the values obtained for S6 are remarkable as seen in Figure 12a. With the increase in current rate, the obtained discharge capacitance is quite constant without much loss. This is due to the high utilization of the surface and fast ion transportation along with the formation of the surface functionalized groups with heteroatoms (P and O) resulting in surface wettability and pseudo-capacitance.[53] This is also further confirmed by the Nyquist plots shown in Figure 12b, and the insets show the magnified high-frequency region and the equivalent circuit. The equivalent series resistance (ESR) of the S6 electrode is as low as 0.4 Ω and there is no visible diameter of the semicircle at high frequencies, which confirms the lower resistance of the charge transport at the electrode surface. The magnified high-frequency region shows a very distorted image with a low charge transfer resistance giving the electrode and current collector interface (Ri) and its corresponding capacitance represented by Ci. Rs represents the electrolyte solution resistance. A short 45° line transitioning into the bent line of the imaginary part of the impedance in the low-frequency region represents a capacitive behavior (C). The particular feature of the Bode frequency plot (Figure S4(A)) shows the variation of impedance exponentially to the frequency. The observed lower impedance showed that the conductivity of sample S6 is high, resulting in the observed high capacitance values. Figure S4(B) shows the Bode plot for sample S6, it is observed that the phase angle is approximately −30° at 1 Hz, which deviates from the ideal EDLC behavior angle of −90° at low frequencies. This is also evidenced in the CV and CD curves, due to the pseudocapacitive in nature. The HDP-AC samples

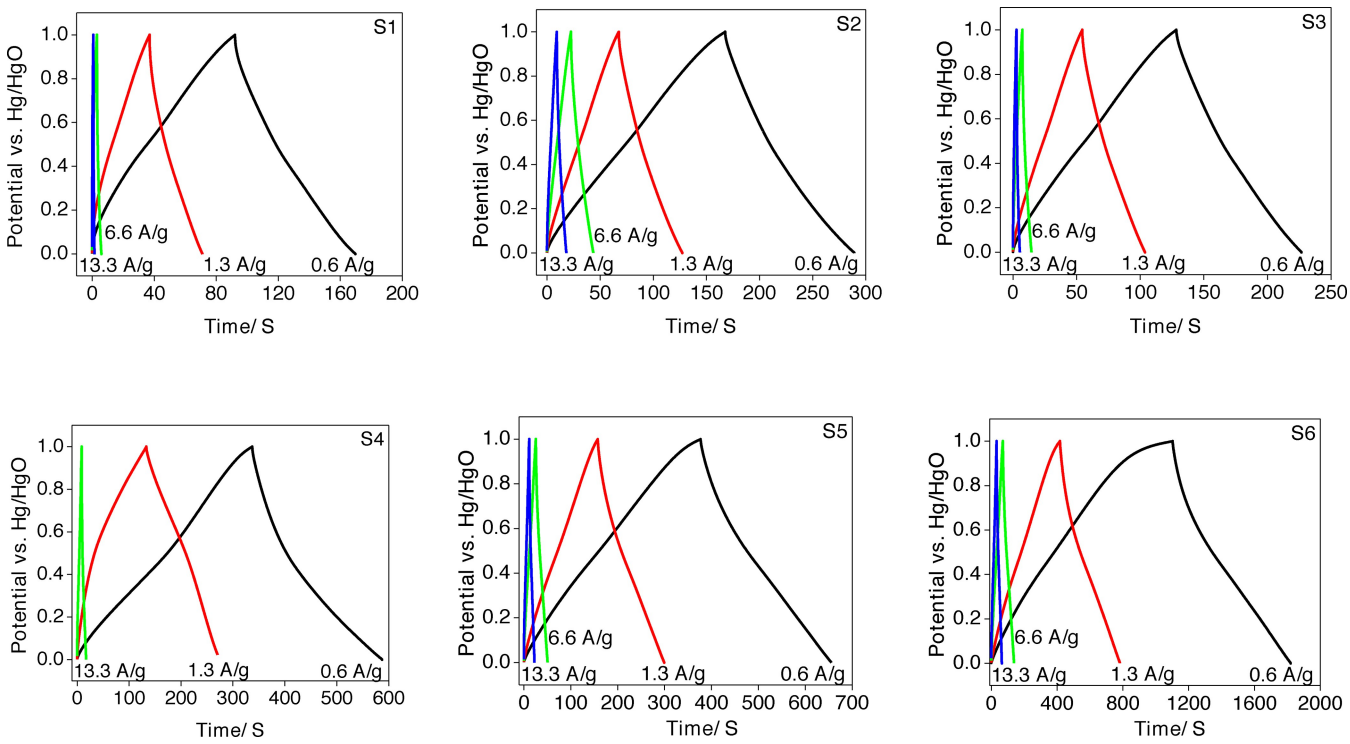

Figure 11. Charge-discharge (CD) curves for the activated carbon sample derived from the honeydew peel (HDP-AC) tested in 1MH_2SO_4 at various current densities shown in the respective figures.

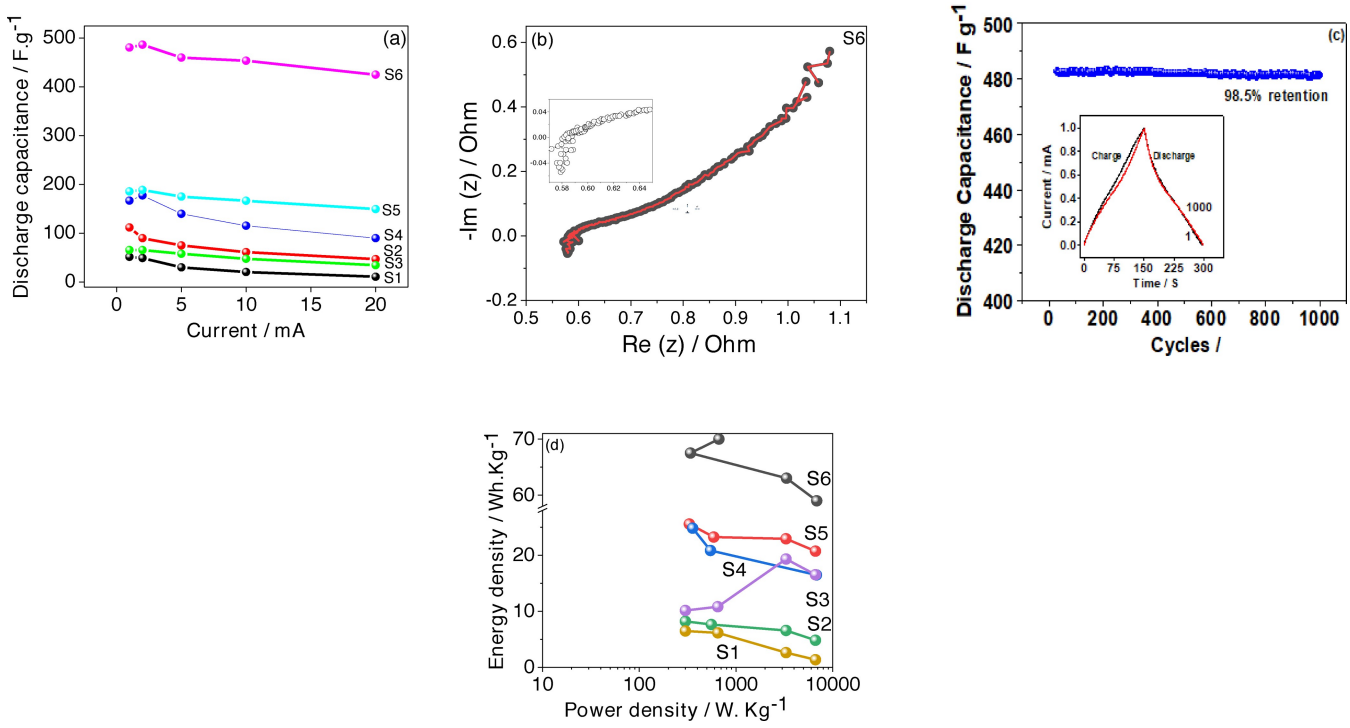

Figure 12. Performance metrics of the S6 activated carbon sample derived from the honeydew peel (HDP-AC) tested in 1MH_2SO_4. (a) Variation of discharge capacitance with current for various compositions, (b) Nyquist plot and the insets show the magnified high-frequency region with a distorted semicircle and the equivalent circuit used for curve fitting, (c) cycling stability with the inset showing the charge-discharge curves superimposed for the cycles 1 and 1000, and (d) Ragone plot of the S1–S6 samples derived from the HDP-AC.

demonstrated a non-ideal capacitive performance as seen in both the Nyquist and Bode plots. The effect of the impregnation ratio and activation temperature[25] determines the yield of HDP-AC, and its pseudocapacitive behavior in sample S6 exhibiting the best performance. The coulombic efficiency of the cell is between 90–98% tested at various current densities (shown in Figure S3), which indicates the electrochemical stability of the HDP-AC-derived sample S6. Based on this, the median value of 3.3 A/g has been chosen for the long-term cycling test to maximize the performance without any deterioration in the charge-transfer processes at the interfaces. The chosen value is a trade-off between the coulombic efficiency and the capacitance retention.

The long-term cycling performance of the HDP-AC was conducted using charge-discharge measurements at a current density of 3.3 A/g. Figure 12c shows the specific capacitance retention versus cycle number for the HDP-AC S6 sample. The specific capacitance is stable, with an excellent retention of 98.5% of its initial value. This high-performance behavior is attributed to physicochemical characteristics such as the presence of heteroatoms containing groups of HDP-derived activated carbon. During the thermal decomposition of HDP under ambient synthesis conditions, heteroatoms played a key role in effectively blocking the formation of levoglucosan ($C_6H_{10}O_5$, a highly volatile).[54–55] This stabilized the HDP-AC electrode to accommodate ions reversibly and enable long-term cycling performance.

The performance metrics of the activated carbon synthesized from various biomass precursors have been compared. From Table 4, for activated carbon derived from various biomass precursors, the specific capacitance obtained for our current work in HDP in 1 M H_2SO_4 acid electrolyte is significantly higher at 480 F g^{-1} than those in reported other precursors in various aqueous electrolytes[15,20,35,56–73] at an energy density of 66.5 Wh/kg and a maximum power density of 662 W/kg. Previous studies have also shown there is a relationship between the specific capacitance of the activated carbons and the chosen electrolyte.[74–76] This can be understood by considering the ion mobility which is closely related to the electrolyte conductivity.[77–78] For EDLCs with a strong acid electrolyte such

Table 4. Summary of the performance metrics of biomass-derived AC materials as SCs in aqueous electrolytes.

Biomass precursors [Ref.]	Voltage (V)	Electrolyte	Current density	Specific capacitance (F/g)	Energy density (Wh/kg)	Power density (W/kg)
Lotus calyx[20]	1	6 M KOH	1 A/g	223	66.8	800
Mango seed[15]	1	2 M NaOH	5 mA/cm^2	135	19	1077
Groundnut Shell[56]	1	6 M KOH	0.5 A/g	220.6	7.64	275
	1.8	0.5 M Na_2SO_4	0.5 A/g	150.4	16.92	451.2
Corn Starch[57]	1	6 M KOH	0.625 A/g	144	19.9	311
Kusha grass (Desmostachya bipinnata)[58]	0.8	6 M KOH	0.7 A/g	218	19.3	277.92
Neem (azadirachta indica)[59]	2	1 M $LiClO_4$	1 mA/cm^2	74.41	10.33	4660
Sunflower Stalk[60]	1	6 M KOH	0.5 A/g	263	35.7	989
Rockmelon Peel[35]	1	1 M KOH	1 A/g	404	29.3	279.78
Bamboo[61]	1	6 M KOH	0.1 A/g	258	>2	>2000
Pine Cone[62]	2	1 M Na_2SO_4	0.1 A/g	137	19	100
Borassus flabellifer flower[63]	0.6	1 M KOH	1 A/g	238.2	–	–
Camellia oleifera shell[64]	1	1 M H_2SO_4	0.2 A/g	374	–	–
	1	6 M KOH	0.2 A/g	266	–	–
Lentinus edodes[65]	1	1M H_2SO_4	0.2 A/g	389	54.03	–
Peanut shell[66]	1	1 M H_2SO_4	0.5 A/g	340	10.8	106.9
Tamarindus indica Fruit Shell[67]	0.78	1 M KOH	1 A/g	285	–	–
Oil palm empty fruit bunches[68]	1	1 M H_2SO_4	–	150	4.3	173.3
Rice Straw	1	6 M KOH	0.5 A/g	178	–	–
Rice Straw – N doped[69]				324 @N-doped	–	–
Cotton[70]	1	6 M KOH	0.5 A/g	270	18	250
Ginkgo leaves[71]	1	1M H_2SO_4	0.5 A/g	374	45.9	221
Pomelo Peel[72]	1.7	1 M $NaNO_3$	0.5 A/g	43.5	17.1	420
Sugar cane bagasse[73]	1	1 M H_2SO_4	0.25 A/g	$\backsim$300	5.9	10 000
Honeydew Peel HDP (This work)	1	1M H_2SO_4	0.6 A/g	480	66.5	662

as H_2SO_4, the reported specific capacitances in Table 4 are mainly in the range between 150 and 350 $F g^{-1}$, which are generally lower than those obtained for our work in HDP-AC electrodes.

The power and energy trade-off for the various compositions of HDP-AC samples (S1–S6) is captured in the so-called "Ragone plot", shown in Figure 12d. The HDP-AC samples overall pushed the limits of the power density to the lower right-hand corner of the plot but interestingly, the best-performed sample S6 achieved the purpose of this work on moving the supercapacitor performance to the upper right-hand corner of this plot. This implies the heteroatom dopant aids in expanding the Ragone plot. This sort of high-power capacitive storage 6850 W/Kg at 59 Wh/kg delivered by sample S6 could be used to impel the vehicle during acceleration at a longer range, for which high-power operation is essential. This characteristic makes HDP-AC a promising candidate for applications where energy density is crucial.

Conclusions

A low-cost, high-quality activated carbon material derived from the natural honeydew peel (HDP) biomass is achievable through the appropriate selection of synthesis conditions. The honeydew (*Cucumis melo Inodorous group*) fruit peel-derived activated carbon (HDP-AC) had been successfully prepared at the optimal combination of carbonized HDP to H_3PO_4 ratio (1 : 4) and activation temperature of 500 °C. The introduction of heteroatoms (P) and oxygen surface functionalities into the cellulose allows for the tuning of electrochemical performance in supercapacitors. The various factors including the concentration of the acid activator phosphoric acid (H_3PO_4), its impregnation ratio, and activation temperature greatly influenced the HDP-AC yield and its pores. The HDP-AC sample tested in the KOH electrolyte showed electric double-layer capacitance while the H_2SO_4 electrolyte under identical conditions showed pseudo-faradaic reactions involving the surface functional groups in the activated carbon electrode. Further optimizations to HDP and H_3PO_4 ratios along with temperature can provide opportunities to continuously enhance the performance metrics of supercapacitors. The single electrode configuration of HDP-AC was able to exhibit a specific capacitance of 480 F/g at an energy density of 66.5 Wh/kg and a maximum power density of 662 W/kg.

Acknowledgements

M. M. acknowledges the Winston Churchill Memorial Trust to learn globally and inspire locally. This work was partially supported by the Japan Society for the Promotion of Science (JSPS) KAKENHI Grant Numbers JP20H00392 and JP23H05459. Open Access publishing facilitated by Murdoch University, as part of the Wiley - Murdoch University agreement via the Council of Australian University Librarians.

Conflict of Interests

The authors declare no conflict of interest.

Data Availability Statement

The data that support the findings of this study are available from the corresponding author upon reasonable request.

Keywords: honeydew · fruit · peel · porous · biomass · carbon · capacitor

[1] D. L. Stern, A. Kander, *The Energy Journal* **2012**, *33* (3), 125–152.
[2] K. Abbass, M. Z. Qasim, H. Song, M. Murshed, H. Mahmood, I. Younis, *Environ. Sci. Pollution Res.* **2022**, *29* (28), 42539–42559.
[3] M. Farghali, A. I. Osman, Z. Chen, A. Abdelhaleem, I. Ihara, I. M. A. Mohamed, P.-S. Yap, D. W. Rooney, *Environ. Chem. Lett.* **2023**, *21*, 1381–1418.
[4] M. J. B. Kabeyi, O. A. Olanrewaju, *Front. Energy Res.* **2022**, *9*, 743114.
[5] I. Dincer, *Renewable Sustainable Energy Rev.* **2000**, *4* (2), 157–175.
[6] P. Ralon, M. Taylor, A. Ilas, K.-P. Kairies, *International Renewable Energy Agency (IRENA)*, Abu Dhabi, **2017**.
[7] C. Liu, F. Li, L.-P. Ma, H.-M. Cheng, *Adv. Mater.* **2010**, *22* (8), E28–E62.
[8] J. Mitali, S. Dhinakaran, A. A. Mohamad, *Energy Storage and Saving* **2022**, *1* (3), 166–216.
[9] B. Pal, S. Yang, S. Ramesh, V. Thangadurai, R. Jose, *Nanoscale Adv.* **2019**, *1*, 3807–3835.
[10] Y. Gogotsi, P. Simon, *Science* **2011**, *334*, 917–918.
[11] L. M. Da Silva, R. Cesar, C. M. R. Moreira, J. H. M. Santos, L. G. De Souza, B. M. Pires, R. Vincentini, W. Nunes, H. Zanin, *Energy Storage Mater.* **2020**, *27*, 555–590.
[12] E. Antolini, *Renewable Sustainable Energy Rev.* **2016**, *58*, 34–51.
[13] H. Yang, H. Guo, K. Pang, P. Fan, X. Li, W. Ren, R. Song, *Nanoscale* **2020**, *12*, 7024–7034.
[14] Z. M. Yunus, N. Othman, A. Al-Gheethi, R. Hamdan, N. N. Ruslan, *J. Dispersion Sci. Technol.* **2021**, *42* (5), 715–729.
[15] W. A. M. K. P. Wickramaarachchi, X. Gao, R. Dabare, K. W. Wong, *Chem. Engg. Journal Adv.* **2021**, *8*, 100158.
[16] P. L. Xiaojun He, M. Yu, X. Wang, X. Zhang, M. Zheng, *Electrochim. Acta* **2013**, *105*, 635–641.
[17] Y. Z. Ru-Juan Moab, M. Wu, H.-M. Xiao, S. Kuga, Y. Huang, J.-P. Li, S.-Y. Fuc, *RSC Adv.* **2016**, *6* (64), 59333–59342.
[18] A. Adan-Mas, L. Alcaraz, P. Arévalo-Cid, F. A. López-Gómez, F. Montemor, *Waste Management* **2021**, *120*, 280–289.
[19] D. Lan, M. Chen, Y. Liu, Q. Liang, W. Tu, Y. Chen, J. Liang, F. Qiu, *J. Mater. Sci. Mater. Electron.* **2020**, *31* (21), 18541–18553.
[20] G. Dhakal, D. Mohapatra, Y.-I. Kim, J. Lee, W. K. Kim, J.-J. Shim, *Renewable Energy* **2022**, *189*, 587–600.
[21] B. Xu, Y. Chen, G. Wei, G. Cao, H. Zhang, Y. Yang, *Mater. Chem. Phys.* **2010**, *124* (1), 504–509.
[22] T. E. Rufford, D. Hulicova-Jurcakova, Z. Zhu, G. Q. Lu, *Electrochem. Commun.* **2008**, *10*, 1594–1597.
[23] C. Wang, L. Sun, Y. Zhou, P. Wan, X. Zhang, J. Qiu, *Carbon* **2013**, *59*, 537–546.
[24] S. Lu, L. Fang, X. Wang, T. X. Liu, X. Zhao, B. B. Xu, Q. Hua, H. Liu, *Mater. Today Chem.* **2024**, *37*, 101988.
[25] R. Zakaria, N. A. Jamalluddin, M. Z. Abu Bakar, *Results in Mater.* **2021**, *10*, 100183.
[26] J. Zhou, S. Zhang, Y.-N. Zhou, W. Tang, J. Yang, C. Peng, Z. Guo, *Electrochem. Energy Reviews* **2012**, *4*, 219–248.
[27] H. Liu, S. Liu, L. Liu, *Adv. Mater. Sci. Technol.* **2023**, *5* (1), 0511809.
[28] S. M. Yakout, G. Sharaf El-Deen, *Arabian Journal of Chem.* **2016**, *9*, S1155–S1162.
[29] J. R. Rajabathar, M. Sivachidambaram, J. J. Vijaya, H. A. Al-lohedan, D. M. D. Aldhayan, *ACS Omega* **2020**, *5* (25), 15028–15038.
[30] A. Elmouwahidi, E. Bailón-García, A. F. Pérez-Cadenas, F. J. Maldonado-Hódar, F. Carrasco-Marín, *Electrochim. Acta* **2017**, *229*, 219–228.
[31] H. Si, B. Wang, H. Chen, Y. Li, X. Zhang, X. Liang, L. Sun, S. Yang, D. Hou, *Int. J. Electrochem. Sci.* **2019**, *14* (8), 7899–7910.

[32] Y. Liu, et al., *J. Electroanal. Chem.* **2021**, *903* (15), 115828.
[33] M.-C. Liu, L.-B. Kong, P. Zhang, Y.-C. Luo, L. Kang, *Electrochim. Acta* **2012**, *60*, 443–448.
[34] N. Jorge, A. Carolina da Silva, C. M. Veronezi, Antioxidant and pharmacological activity of Cucumis melo var. cantaloupe (Ch. 13) in a Book "Multiple Biological Activities of Conventional Seed Oils" Ed. A. A. Mariod (Academic Press), **2022**, 147–150.
[35] E. Elaiyappillai, R. Srinivasan, Y. Jonbosco, P. Devakumar, K. Murugesan, K. Kesavan, P. M. Johsnon, *Appl. Surf. Sci.* **2019**, *486*, 527–538.
[36] M. Yunus, A. Al-Gheethi, N. Othman, R. Hamdan, N. N. Ruslan, *J. Cleaner Prod.* **2020**, *251*, 119738.
[37] M. Jagtoyen, F. Derbyshire, *Carbon* **1998**, *36* (7–8), 1085–1097.
[38] R. Gomez-Garcio, D. A. Campos, A. Oliveira, C. N. Aguilar, A. R. Madureira, M. Pintado, *Food Chem.* **2021**, *335*, 127579.
[39] Y. Huang, H. Liu, H. Yuan, X. lv, B. Xu, W. Li, J. Uttauean, X. Yin, C. Wu, *Fuel* **2020**, *227*, 118205.
[40] B. Chen, W. Wu, C. Li, Y. Wang, Y. Zhang, L. Fu, Y. Zhu, L. Zhang, Y. Wu, *Sci. Reports* **2019**, *9*, 5431.
[41] Y. P. Wu, S. B. Fang, Y. Y. Jiang, *J. Mater. Chem.* **1998**, *8*, 2223–2227.
[42] S. Pap, T. S. Knudsen, J. Radonic, S. Maletic, S. M. Iqic, M. T. Sekulic, *J. Cleaner Prod.* **2017**, *162*, 958–972.
[43] W. Qian, F. Sun, Y. Xu, L. Qiu, C. Liu, S. Wang, F. Yan, *Energy Environ. Sci.* **2014**, *7*, 379–386.
[44] Z. Zhao, S. Hao, P. Hao, Y. Sang, A. Manivannan, N. Wu, H. Liu, *J. Mater. Chem. A* **2015**, *3*, 15049–15056.
[45] M. Liu, J. Niu, Z. Zhang, M. Dou, F. Wang, *Nano Energy* **2018**, *51*, 366–372.
[46] F. Suarez-Garcia, S. Villar-Rodil, C. G. Blanco, A. Maryinez-Alonso, J. M. D. Tarascon, *Chem. Mater.* **2004**, *16*, 2639–2647.
[47] A. M. Puziy, O. I. Poddubnaya, A. Martinez-Alonso, F. Suarez-Garcia, J. M. D. Tarascon, *Carbon* **2005**, *43*, 2857–2868.
[48] K. Kierzek, G. Gryglewicz, *Molecules* **2020**, *25* (18), 4255.
[49] F. Ambroz, T. J. Macdonald, V. Martis, I. V. Parkin, *Small Methods* **2018**, *2* (11), 1800173.
[50] C. Zhong, Y. Deng, W. Hu, J. Qiao, L. Zhang, J. Zhang, *Chem. Soc. Rev.* **2015**, *44*, 7784–7539.
[51] G. Lin, Q. Wang, X. Yang, Z. Cai, Y. Xiong, B. Huang, *RSC Adv.* **2020**, *10*, 17768–17776.
[52] D. Wang, Z. Geng, B. Li, C. Zhang, *Electrochim. Acta* **2015**, *173*, 377–384.
[53] F. Wang, J. Y. Cheong, Q. He, G. Duan, S. He, L. Zhang, Y. Zhao, I.-D. Kim, S. Jiang, *Chem. Engg. J.* **2021**, *414*, 128767.
[54] A. L. Sullivan, R. Ball, *Atmospheric Environ.* **2012**, *47*, 133–141.
[55] E. H. Ablouh, F. Brouillette, M. Taourrite, H. Sehaqui, M. El Achaby, A. Belfkira, *RSC Adv.* **2021**, *11* (39), 24206–24216.
[56] M. Muthu Balasubramanian, M. Subramani, D. Murugan, S. Ponnusamy, *Ionics* **2020**, *26* (12), 6297–6308.
[57] L. Pang, B. Zou, Y. Zou, X. Han, L. Cao, W. Wang, Y. Guo, *Colloids Surf. A* **2016**, *504*, 26–33.
[58] G. K. Gupta, P. Sagar, S. K. Pandey, M. Srivastava, A. K. Singh, J. Singh, A. Srivastava, S. K. Srivastava, A. Srivastava, *Nanoscale Res. Lett.* **2021**, *16* (1), 85.
[59] S. Ahmed, M. Parvaz, R. Johari, M. Rafat, *Mater. Res. Express* **2018**, *5* (4), 045601.
[60] X. Wang, S. Yun, W. Fang, C. Zhang, X. Liang, Z. Lei, Z. Liu, *ACS Sustainable Chem. Eng.* **2018**, *6* (9), 11397–11407.
[61] C.-S. Yang, Y. S. Jang, H. K. Jeong, *Current Appl. Phy.* **2014**, *14* (12), 1616–1620.
[62] A. Bello, N. Manyala, F. Barzegar, A. A. Khaleed, D. Y. Momodu, J. K. Dangbegnon, *RSC Adv.* **2016**, *6* (3), 1800–1809.
[63] M. Sivachidambaram, J. Vijaya, L. J. Kennedy, R. Jothiramalingam, H. A. Ali-Lohedan, M. A. Munusamy, E. Elanthamilan, J. Princy Merlin, *New J. Chem.* **2017**, *41* (10), 3939–3949.
[64] J. Zhang, L. Gong, K. Sun, J. Jiang, X. Zhang, *J. Solid State Electrochem.* **2012**, *16* (6), 2179–2186.
[65] D. Tang, Y. Luo, W. Lei, Q. Xiang, W. Ren, W. Song, K. Chen, J. Sun, *Appl. Surf. Sci.* **2018**, *462*, 862–871.
[66] Z. Xiao, W. Chen, K. Liu, P. Cui, D. Zhan, *Int. J. Electrochem. Sci.* **2018**, *13* (6), 5370–5381.
[67] M. Sivachidambaram, J. Vijaya, K. Niketha, L. Kennedy, E. Elaiyappillai, J. Merlin, *J. Nanoscience and Nanotechnology* **2019**, *19* (6), 3388–3397.
[68] R. Farma, M. Deraman, A. Awitdrus, I. A. Talib, E. Toer, N. H. Basri, I. G. Manunatha, M. M. Ishak, B. N. M. Dollah, S. A. Hashmi, *Bioresour. Technol.* **2013**, *132*, 254–261.
[69] K. Charoensook, C.-L. Huang, H.-C. Tai, V. V. Krishna Lanjapalli, L.-M. Chiang, S. Hosseini, Y.-T. Lin, Y.-Y. Li, *Journal of the Taiwan Institute of Chemical Engineers* **2021**, *120*, 246–256.
[70] L. Zhang, L. Xu, Y. Zhang, X. Zhou, L. Zhang, A. Yasin, L. Wang, K. Zhi, *RSC Adv.* **2018**, *8* (7), 3869–3877.
[71] X. Zhu, S. Yu, Y. Zhang, L. Zhang, G. Lou, Y. Wu, E. Zhu, H. Chen, Z. Shen, B. Boo, S. Fu, *Chem. Engg. Sci.* **2018**, *181*, 36–45.
[72] C. Peng, J. Lang, S. Xu, X. Wang, *RSC Adv.* **2014**, *4* (97), 54662–54667.
[73] T. E. Rufford, D. Hulicova-Jurcakova, K. Khosla, Z. Zhu, G. Q. Lu, *J. Power Sour.* **2010**, *195* (3), 912–918.
[74] J. B. Franklin, S. Sachin, S. John Sundaram, G. Theophil Anand, A. Dhayal Raj, K. Kaviyarasu, *Mater. Sci for Energy Technol.* **2024**, *7*, 91–98.
[75] G. Theopjil Anand, D. Renuka, R. Ramesh, L. Anandaraj, S. John Sundaram, G. Ramalingam, C. Maria Magdalene, A. K. H. Basir, M. Maaza, K. Kavaiyarasu, *Surfaces and Interfaces* **2019**, *17*, 100376.
[76] A. Sudha, N. M. I. Alhaji, A. Ayeshamariam, M. Ismail Fathima, M. Sivabharathy, K. Kaviyarasu, *Mater. Sci for Energy Technol.* **2022**, *5*, 424–432.
[77] M. Venkatachalatahy, K. Sambathkumar, M. E. Rajasaravanan, R. Uthrakumar, K. Kaviyarasu, M. A. Yewale, M. Awad, M. W. Alam, *Luminescence* **2024**, *39*, e4768.
[78] A. M. Amanullah, C. Maria Magdalene, S. Saranya, R. Sundaram, K. Kaviyarasu, *Surfaces and Interfaces* **2021**, *22*, 100835.

Manuscript received: May 31, 2024
Revised manuscript received: July 2, 2024
Accepted manuscript online: July 2, 2024
Version of record online: August 21, 2024